• Article •

Steady state response of an infinite beam on a viscoelastic foundation with moving distributed mass and load

Yin Zhang[1,2*]

[1]*State Key Laboratory of Nonlinear Mechanics (LNM), Institute of Mechanics, Chinese Academy of Sciences, Beijing 100190, China;*
[2]*School of Engineering Science, University of Chinese Academy of Sciences, Beijing 100049, China*

Compared with the moving concentrated load model, it is more realistic and proper to use the moving distributed mass and load model to simulate the dynamics of a train moving along a railway track. In the problem of a moving concentrated load, there is only one critical velocity, which divides the load moving velocity into two categories: subcritical and supercritical. The locus of a concentrated load demarcates the space into two parts: the waves in these two domains are called the front and rear waves, respectively. In comparison, in the problem of moving distributed mass and load, there are two critical velocities, which results in three categories of the distributed mass moving velocity. Due to the presence of the distributed mass and load, the space is divided into three domains, in which three different waves exist. Much richer and different variation patterns of wave shapes arise in the problem of the moving distributed mass and load. The mechanisms responsible for these variation patterns are systematically studied. A semi-analytical solution to the steady-state is also obtained, which recovers that of the classical problem of a moving concentrated load when the length of the distributed mass and load approaches zero.

steady state, beam, viscoelastic foundation, moving distributed mass

PACS number(s):   02.30.Oz, 46.40.-f, 46.40.Ff, 46.70.De

1   Introduction

The steady state solution of an infinite beam on an elastic foundation under a moving concentrated load was first obtained, in connection with the stress analysis of railway tracks, by Timoshenko in 1926 [1]. Timoshenko found that there is a critical velocity at which the vibration amplitude of the undamped beam approaches infinity [1]. This critical velocity is found to be around 1800 km/h [1, 2], which is much larger than the highest train speed at that time and nowadays. At a first look, the dynamic effect should be little because of this very high critical velocity [3]. While, this moving load induced vibration can cause very significant dynamic

effect in conjunction with the track irregularities [4-6]. Recent analysis shows that the difference between the static and dynamic wheel-track contact stress can be as large as twenty times [5]. Nowadays the continuous welded rail (CWR) is widely used in modern railways. Because of the complete elimination of expansion joints in the CWR tracks, the thermal stresses due to the rising temperature can cause considerable axial compression, which leads to a significantly lower critical velocity or even buckling [3]. In fact, the possibility of the track buckling due to compressive thermal stress was the main reason for delaying the use of CWR track by decades [3]. And actually, a large number of the train accidents are due to the track buckling instability [7]. Besides the compressive axial load, a soft foundation can further reduce

*Corresponding author (email: zhangyin@lnm.imech.ac.cn)

the critical velocity. For example, the critical velocity is only 169 km/h for a peat foundation [8] and 290-338 km/h for a poroelastic foundation [9,10]. It is not unusual that a modern high-speed train exceeds the critical velocity [11]. Even as early as the 1950s, this critical velocity was easily surpassed by a rocket-propelled vehicle on a test track [12]. The dynamic effects due to the rapidly moving load/mass become more and more important for the developments of high-speed trains.

Physically, the moving concentrated load is to model the wheel-track contact load of a moving vehicle. Most studies adopted the model of a beam on an elastic foundation under one moving concentrated load [1, 3, 11-14]. For a linear model of a beam on an elastic foundation, the superposition rule applies [15, 16] and therefore, the extension to the case with multiple concentrated loads can be relatively easily carried out. The examples of the two-concentrated-load case to model a bogie and the four-concentrated-load case to model a wagon were given by Vostroukhov and Metrikine [17]. However, in the moving load model the mass/inertia effect of a moving vehicle is not incorporated [18-20] and the moving mass problem is much more difficult than that of a moving load [20]. Several models of a moving concentrated mass have been proposed [18-20]. In Duffy's model of a moving concentrated mass together with a concentrated driving harmonic load, the resonance occurs at a lower driving frequency for a larger moving concentrated mass [18]. Metrikine and Dieterman's results showed that with a larger concentrated mass, a smaller supercritical velocity can cause instability [19]. Dimitrovová showed that the natural frequency of the beam/foundation system varies differently depending on the magnitude of the moving concentrated mass [20]. While, all these three models of an infinite beam show that the magnitude of a moving concentrated mass has no impact on the critical velocity [18-20], which is determined only by the beam stiffness, foundation modulus and axial load [3,19,20]. In contrast to the above infinite beam cases [18-20], we see that in a finite beam with one or several moving concentrated masses, the critical velocity becomes monotonically smaller with the larger moving mass(es) [21, 22]. Esmailzadeh and Ghorashi [23] proposed the model of a finite hinged-hinged beam with a distributed mass to simulate the scenario of a train passing a bridge. The concentrated mass model is shown to be a special case of the distributed mass model [23]. However, as pointed out by Lin [24], the centripetal and Coriolis acceleration terms due to the effect of a moving mass are missing in Esmailzadeh and Ghorashi's model [23], which may lead to questionable or even misleading results. For the finite beam model, the modal analysis, which is a convenient computation tool, can be applied [20-23]. However, the convergence of modal analysis is quite low and a very large number of modes (often more than 100) are required [20]. Furthermore, the perturbations induced by the boundary conditions and reflections of traveling waves in a finite beam model may cause a significant deviation from that of an infinite beam. As a result, in the real applications of train-track dynamics, the model of an infinite beam on an elastic foundation is preferred or even required [13].

For a distributed mass moving along an infinite beam, besides the mass effect, it also causes the effect of a moving distributed load due to gravity. In this study, the model of an infinite beam on a viscoelastic foundation under a moving distributed mass and load is proposed to study the steady-state of a moving train. In this model, the effects of the axial load and those missing acceleration terms in ref. [23] are considered. A semi-analytical solution, which does not involve any numerical discretization procedure, is also presented. Because of the moving mass effect, there is one more critical velocity lower than the one as given by the moving concentrated load model. These two velocities, which are referred to as the critical upper and lower velocities, demarcate three velocity zones for a moving distributed mass and load: subcritical, transcritical and supercritical regions, in which the qualitative differences of wave shapes arise. Our model shows that the critical upper velocity is independent of the moving distributed mass, which agrees with the above cases of the moving concentrated mass(es) on an infinite beam [18-20]; while, the critical lower velocity decreases monotonically with the increase of the moving distributed mass, which agrees with the above cases the moving concentrated mass(es) on a finite beam [21,22]. The present model also confirms that the effect of the critical lower velocity, or say, the effect of the moving distributed mass vanishes when the length of the distributed mass approaches zero, which becomes a concentrated one. The use of the ballastless railway significantly improves the foundation modulus [25] and a much higher critical upper velocity is thus achieved. As shown later, this critical upper velocity can be easily higher than 2000 km/h. However, with the consideration of the effects of a distributed mass and axial compression, the critical lower velocity can be smaller than the operating speed of the nowadays high-speed train, i.e., the train speed is in the transcritical region. The present model of a moving distributed mass shows a significantly different steady-state from that of a moving concentrated load, which can be of some help to a more accurate evaluation of the track vibration and stress.

2 Model development

As shown in Figure 1, a uniformly distributed mass moves along an axially loaded Euler-Bernoulli beam on a viscoelas-

tic Winkler foundation. Here the Euler-Bernoulli model of a slender beam is adopted because the beam is modeled to be infinitely long in order to avoid the effect of wave reflection [13]. In conjunction with the moving mass/load models in refs. [12,19,23], the corresponding governing equation for the beam vibration is given as the following:

$$
EI\frac{\partial^4 y_1}{\partial x_1^4} + N\frac{\partial^2 y_1}{\partial x_1^2} + \{m_1 + m_2[H(x_1 - vt + l/2) \\
- H(x_1 - vt - l/2)]\}\frac{\partial^2 y_1}{\partial t^2} + c\frac{\partial y_1}{\partial t} + ky_1 \\
= m_2g[H(x_1 - vt + l/2) - H(x_1 - vt - l/2)],
$$
(1)

where E, I and m_1 are the beam Young's modulus, area moment of inertia and mass per unit length, respectively. As shown in Figure 1, $y_1 = y_1(x_1, t)$ is the beam transverse displacement as observed in a stationary coordinate system. The beam is under an axial load of N and here a positive/negative N means compression/tension. The Winkler foundation is with the damping of c and modulus of k. Here the damping is a viscous one and the hysteretic damping model on the elastic foundation can be found in ref. [26]. The distributed mass is with the mass per unit length of m_2, length of l and a constant moving velocity of v. H is the Heaviside unit function defined as follows:

$$
H(x_1) = \begin{cases} 0, & x_1 < 0, \\ 1, & x_1 > 0. \end{cases}
$$
(2)

In eq. (1), $m_2[H(x_1 - vt + l/2) - H(x_1 - vt - l/2)]$ and $m_2g[H(x_1 - vt + l/2) - H(x_1 - vt - l/2)]$, are the distributed mass and the transverse distributed load due to its gravity, respectively. Therefore, eq. (1) is the problem of the moving distributed mass and load. In order to have a convenient examination on the results, for example, a comparison with the static one, it is desirable and a common practice to transpose the coordinate system so that it is attached to the moving
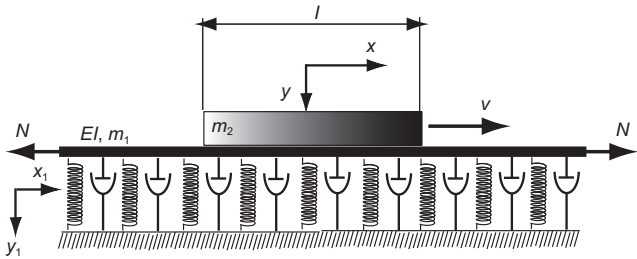
Figure 1   Schematic diagram of a uniformly distributed mass (m_2) moving along a beam supported by a viscoelastic foundation with the modulus of k and damping of c. The beam is under an axial load of N; EI and m_1 are the beam bending stiffness and mass per unit length, respectively. The moving distributed mass is with a constant speed of v and the length of l. The moving coordinate system is at the center of the distributed mass.

mass/load [3,12,23,27]. The following Galiean transformation is introduced

$$
\begin{cases} x = x_1 - vt, \\ y(x) = y_1(x_1 - vt). \end{cases}
$$
(3)

As the distributed mass is moving along a vibrating path, its velocity and acceleration in the constantly moving coordinate system are now expressed as follows [24,27]:

$$
\begin{cases} \dfrac{\partial y_1}{\partial t} = \dfrac{\partial y}{\partial t} - v\dfrac{\partial y}{\partial x}, \\ \dfrac{\partial^2 y_1}{\partial t^2} = \dfrac{\partial^2 y}{\partial t^2} - 2v\dfrac{\partial^2 y}{\partial x\partial t} + v^2\dfrac{\partial^2 y}{\partial x^2}. \end{cases}
$$
(4)

By substituting $\partial y_1/\partial t$ and $\partial^2 y_1/\partial t^2$ of eq. (4) into eq. (1), the governing equation in the moving coordinate is obtained as the following:

$$
EI\frac{\partial^4 y}{\partial x^4} + N\frac{\partial^2 y}{\partial x^2} + \{m_1 + m_2[H(x + l/2) - H(x - l/2)]\} \\
\times \left(\frac{\partial^2 y}{\partial t^2} - 2v\frac{\partial^2 y}{\partial x\partial t} + v^2\frac{\partial^2 y}{\partial x^2}\right) + c\frac{\partial y}{\partial t} - cv\frac{\partial y}{\partial x} + ky \\
= m_2g[H(x + l/2) - H(x - l/2)].
$$
(5)

If the fourth term on the left-hand side of the above equation is set zero, i.e., $m_2[H(x + l/2) - H(x - l/2)] = 0$, eq. (5) recovers the governing equation of the moving distributed load [16]. Clearly, the moving distributed load of $m_2g[H(x + l/2) - H(x - l/2)]$ on the right hand has no impact on the free vibration and thus the stability of the system [16]. The moving load only influences the steady state. Furthermore, the above equation is a linear one in which the superposition rule applies. As a result, various moving load scenarios and their combinations can be rather easily handled [15,16]. In contrast, the axially moving mass affects the stability of the system [27] and thus the critical velocity [19]. Dynamically, eq. (5) is a gyroscopic system due to the effect of the axially moving mass [27] and a gyroscopic system is usually caused by a rotation/spinning [28]. The presence of the moving mass together with the Heaviside function in general poses a harder mathematical problem [21]. It is noteworthy that eq. (5) only describes the transverse vibration and generally, the dynamics/vibration in the horizontal direction is also required to present a full description [29]. The reason why we only study the transverse vibration here is that the transverse and lognitudinal vibrations can be decoupled and the axially moving mass/load has much larger impact on the transverse vibration [27].

For steady-state, all the time-related terms in eq. (5) are gone, which leads to the following equation

$$
EI\frac{\partial^4 y}{\partial x^4} + \{N + m_1v^2 + m_2v^2[H(x + l/2) - H(x - l/2)]\} \\
\times \frac{\partial^2 y}{\partial x^2} - cv\frac{\partial y}{\partial x} + ky = m_2g[H(x + l/2) - H(x - l/2)].
$$
(6)

Because of the vanishing time-varying terms, this steady-state physically means that the beam deformation is stationary relative to the moving coordinate system [30]. While, the moving velocity effect is still (partially) incorporated in the above equation, Frýba called this steady-state quasi-stationary state [31]. In order to nondimensionalize eq. (6), the following dimensional quantities are introduced

$$\lambda = \sqrt[4]{\frac{k}{4EI}}, \; N_{cr} = 2\sqrt{kEI}, \; v_{cr1} = \sqrt[4]{\frac{4kEI}{m_1^2}},$$
$$v_{cr2} = \sqrt[4]{\frac{4kEI}{(m_1 + m_2)^2}}, \; c_r = 2\sqrt{km_1}, \tag{7}$$

here λ is with the unit of m^{-1} and λ^{-1} is a "fundamental length" in the problem of a beam on an elastic foundation [32]. N_{cr} is the buckling load of an infinite beam on an elastic foundation [33]. For a simple spring-mass ($k - m_1$) system, c_r is its critical damping [12]. Here v_{cr1} and v_{cr2} are the two critical velocities for the two infinite beams with the masses per unit length of m_1 and $m_1 + m_2$, respectively. The two critical velocities of v_{cr1} and v_{cr2} are the lowest velocities at which a free wave can propagate [12]. Here a free wave is defined as a wave propagating along the beam without changing its shape [34]. From the viewpoint of vibration, the amplitude of the beam vibration becomes infinite when a critical velocity is reached. This is explained as that the system equivalent stiffness becomes zero at the critical velocity [8]. As seen in eq. (6), the moving masses in conjunction with their velocities, i.e., m_1v^2 and m_2v^2, effectively exert a compressive axial load on the beam. When this effective compressive axial load reaches a critical value, which also corresponds to a critical velocity, the beam buckles [2,3] and the buckling instability corresponds to the zero equivalent stiffness [27].

For the moving load case, two critical velocities are found in the model of a beam on an elastic half space [2,8,10]. In comparison, the model of a beam on an elastic foundation can only result in one critical velocity for the moving load case [2,3]. The above two critical velocities of v_{cr1} and v_{cr2} model is purely due to the moving mass effect. When a load moves on an elastic half-space, there is also only one critical velocity, which is that of the Rayleigh wave. The reason for the appearance of the second critical velocity in the model of a beam on an elastic half space is due to the mass effect of the beam [2,8,10]. This second critical velocity is the critical velocity of the beam bending wave [2], which is the same as the above v_{cr1} and v_{cr2} [11,30]. This second critical velocity is only slightly smaller than that of the Rayleigh wave [2,8,10] and therefore, these two velocities are effectively treated as one [2]. In contrast, the two critical velocities of v_{cr1} and

v_{cr2} as defined in eq. (7) can have a large difference because of the huge difference between m_1 and m_2. Physically, m_1 and m_2 are the masses per unit length of the track and train, respectively. As shown later, these two critical velocities of v_{cr1} and v_{cr2} due to the moving distributed mass play an essential role of determining the beam wave shapes. Because of the large difference between v_{cr1} and v_{cr2}, the model of moving distributed mass and load is believed to capture the train dynamics more accurately than that of moving load. Furthermore, when the elastic foundation modulus (k) is derived by the Biot model [32], the above model of a beam on an elastic foundation predicts the same critical velocity (Rayleigh wave velocity) and buckling load (N_{cr}) as that of a beam on an elastic half space model [2]. It is worth emphasizing that v_{cr1} and v_{cr2} defined in eq. (7) are the critical velocities when the axial load (N) is zero. Besides the properties of the beam and elastic foundation, the critical velocities are also dependent on the axial load [2,3].

The following dimensionless quantities are also introduced:

$$Y = \lambda y, \; \xi = \lambda x, \; L = \lambda l, \; \phi = \frac{N}{N_{cr}}, \; \theta = \frac{v}{v_{cr1}},$$
$$\beta = \frac{c}{c_r}, \; \alpha = \frac{m_2}{m_1}, \; \gamma = \frac{m_2 g \lambda}{k} = \frac{\alpha m_1 g \lambda}{k}, \tag{8}$$

where L is the dimensionless length of the distributed mass of m_2; ϕ, θ and β are its dimensionless axial load, velocity and damping, respectively. Here α is the mass ratio and γ is the dimensionless transverse distributed load exerted by m_2. The two dimensionless critical velocities are given as follows:

$$\theta_{cr1} = \frac{v_{cr1}}{v_{cr1}} = 1, \; \theta_{cr2} = \frac{v_{cr2}}{v_{cr1}} = \sqrt{\frac{1}{1+\alpha}}, \tag{9}$$

here θ_{cr1} is the critical upper velocity and θ_{cr2} is the lower one. Because of the finite length of the distributed mass, the governing equation of eq. (6) is divided into two different equations in three zones as indicated by the Heaviside function. Eq. (6) is now nondimensionalized as follows:

$$\begin{cases} \dfrac{\partial^4 Y}{\partial \xi^4} + 4(\phi + \theta^2)\dfrac{\partial^2 Y}{\partial \xi^2} - 8\theta\beta\dfrac{\partial Y}{\partial \xi} + 4Y = 0, \\ \qquad\qquad \xi < -\dfrac{L}{2} \quad \text{or} \quad \xi > \dfrac{L}{2}, \\ \dfrac{\partial^4 Y}{\partial \xi^4} + 4[(\phi + (1+\alpha)\theta^2]\dfrac{\partial^2 Y}{\partial \xi^2} - 8\theta\beta\dfrac{\partial Y}{\partial \xi} + 4Y = 4\gamma, \\ \qquad\qquad -\dfrac{L}{2} \leq \xi \leq \dfrac{L}{2}. \end{cases} \tag{10}$$

The solutions to eq. (10) are derived in Appendix with the

following forms:

$$Y(\xi) = \begin{cases} Y_1(\xi) = \mathrm{e}^{-a\xi}[C_1 \sin(b_2\xi) + C_2 \cos(b_2\xi)] \\ \qquad + \mathrm{e}^{a\xi}[C_1' \sin(b_1\xi) + C_2' \cos(b_1\xi)], \\ \qquad\qquad\qquad \xi > \dfrac{L}{2}, \\ Y_2(\xi) = \mathrm{e}^{a\xi}[C_3 \sin(b_1\xi) + C_4 \cos(b_1\xi)] \\ \qquad + \mathrm{e}^{-a\xi}[C_3' \sin(b_2\xi) + C_4' \cos(b_2\xi)], \\ \qquad\qquad\qquad \xi < -\dfrac{L}{2}, \\ Y_3(\xi) = \mathrm{e}^{-c\xi}[C_5 \sin(d_2\xi) + C_6 \cos(d_2\xi)] \\ \qquad + \mathrm{e}^{c\xi}[C_7 \sin(d_1\xi) + C_8 \cos(d_1\xi)] + \gamma, \\ \qquad\qquad -\dfrac{L}{2} \le \xi \le \dfrac{L}{2}, \end{cases} \quad (11)$$

here C_is ($i = 1$ to 8) and C_i's ($i = 1$ to 4) are the twelve constants to be determined by the boundary conditions. The exponents of a and c are the positive real roots of the following two equations:

$$a^6 + 2(\phi + \theta^2)a^4 + \left[(\phi + \theta^2)^2 - 1\right]a^2 - \theta^2\beta^2 = 0, \quad (12)$$

$$c^6 + 2[(\phi + (1 + \alpha)\theta^2]c^4 + \left\{\left[\phi + (1 + \alpha)\theta^2\right]^2 - 1\right\}c^2 \\ - \theta^2\beta^2 = 0, \quad (13)$$

The wave numbers of b_1, b_2 and d_1, d_2 are given as follows:

$$\begin{cases} b_1 = \sqrt{2(\phi + \theta^2) + a^2 - 2\dfrac{\theta\beta}{a}}, \\ b_2 = \sqrt{2(\phi + \theta^2) + a^2 + 2\dfrac{\theta\beta}{a}}, \\ d_1 = \sqrt{2[(\phi + (1 + \alpha)\theta^2] + c^2 - 2\dfrac{\theta\beta}{c}}, \\ d_2 = \sqrt{2[(\phi + (1 + \alpha)\theta^2] + c^2 + 2\dfrac{\theta\beta}{c}}. \end{cases} \quad (14)$$

As ξ approaches $\pm\infty$, $C_1' = C_2' = C_3' = C_4' = 0$ must be taken in order to keep the beam deflection of Y finite. Therefore, the solutions to eq. (10) are then changed into the following forms:

$$Y(\xi) = \begin{cases} Y_1(\xi) = \mathrm{e}^{-a\xi}[C_1 \sin(b_2\xi) + C_2 \cos(b_2\xi)], \\ \qquad\qquad\qquad \xi > \dfrac{L}{2}, \\ Y_2(\xi) = \mathrm{e}^{a\xi}[C_3 \sin(b_1\xi) + C_4 \cos(b_1\xi)], \\ \qquad\qquad\qquad \xi < -\dfrac{L}{2}, \\ Y_3(\xi) = \mathrm{e}^{-c\xi}[C_5 \sin(d_2\xi) + C_6 \cos(d_2\xi)] \\ \qquad + \mathrm{e}^{c\xi}[C_7 \sin(d_1\xi) + C_8 \cos(d_1\xi)] + \gamma, \\ \qquad\qquad -\dfrac{L}{2} \le \xi \le \dfrac{L}{2}. \end{cases} \quad (15)$$

Now only eight unknowns of C_is ($i = 1$ to 8) are left. At $\xi = \pm L/2$, the continuity of the displacement, slope, moments and shear gives the following eight equations in total [35]:

$$Y_1\left(\frac{L}{2}\right) = Y_3\left(\frac{L}{2}\right), \ Y_1'\left(\frac{L}{2}\right) = Y_3'\left(\frac{L}{2}\right),$$
$$Y_1''\left(\frac{L}{2}\right) = Y_3''\left(\frac{L}{2}\right), \ Y_1'''\left(\frac{L}{2}\right) = Y_3'''\left(\frac{L}{2}\right), \quad (16)$$

$$Y_2\left(-\frac{L}{2}\right) = Y_3\left(-\frac{L}{2}\right), \ Y_2'\left(-\frac{L}{2}\right) = Y_3'\left(-\frac{L}{2}\right),$$
$$Y_2''\left(-\frac{L}{2}\right) = Y_3''\left(-\frac{L}{2}\right), \ Y_2'''\left(-\frac{L}{2}\right) = Y_3'''\left(-\frac{L}{2}\right). \quad (17)$$

Here $()' = \partial/\partial\xi$. Y_i', Y_i'' and Y_i''' ($i = 1$ to 3) are found by taking the consecutive derivatives of Y_i in eq. (15). With the eight equations provided by eqs. (16) and (17), the eight unknowns of C_is can now be solved.

3 Results and discussion

The following parameters are taken from the high-speed railway track of UIC60 [36]: $E = 2\times10^{11}$ N/m^2, $I = 3.06\times10^{-5}$ m^4 and $m_1 = 60.34$ kg/m. The foundation modulus varies in a large range of 5×10^6 N/m$^2 \le k \le 10^9$ N/m^2 and here a typical value of $k = 1.67 \times 10^7$ N/m^2 is taken [36]. The corresponding quantities defined in eq. (7) are with the following fixed values: $\lambda = 0.8991$ m^{-1}, $N_{cr} = 1.979 \times 10^7$ N, $v_{cr1} = 572.7$ m/s (2061.7 km/h) and $c_r = 62134$ kg m^{-1} s^{-1}.

For a start, the axial load is set to be zero, i.e., $\phi = 0$. The effect of the axial load will be addressed later in details. The effects of the train length (L), velocity (θ), damping (β), mass (α) and load (γ) are firstly examined. In Figure 2, we compute the first case of $\alpha = 50$ and $L = 2 \times 10^{-3}$. Here the very small L is taken to simulate the concentrated load and mass scenario. The wave shapes of $\theta = 0$, $\theta = 1$ and $\theta = 2$ with the damping fixed as $\beta = 0.1$ are plotted in Figure 2. The wave shapes of $\theta = 0$, $\theta = 1$ and $\theta = 2$ for a moving concentrated load problem with $\beta = 0.1$ are also computed by Kenney [12]. The comparison between our wave shapes and Kenney's [12] shows that they are the same. Physically, there is the moving (distributed) mass effect as embodied in the $4(1 + \alpha)\theta^2]\partial^2 Y/\partial\xi^2$ term of eq. (10) in our model and there is none in Kenney's model [12]. Why our model predicates the same wave shapes as Kenney's is explained in the next paragraph. Furthermore, our $\theta = 0$ case also exactly matches the analytical solution of the (dimensionless) track/beam static deflection on an elastic foundation under a distributed load, which is given as follows [33]:

$$Y(\xi) = \begin{cases} Y_1(\xi) = -\dfrac{\gamma}{2}\left[\mathrm{e}^{-(L/2+\xi)}\cos(L/2 + \xi) \right. \\ \qquad \left. + \mathrm{e}^{-(-L/2+\xi)}\cos(-L/2 + \xi)\right], \\ \qquad\qquad\qquad \xi > \dfrac{L}{2}, \\ Y_2(\xi) = \dfrac{\gamma}{2}\left[\mathrm{e}^{(L/2+\xi)}\cos(L/2 + \xi) \right. \\ \qquad \left. + \mathrm{e}^{-(L/2-\xi)}\cos(L/2 - \xi)\right], \\ \qquad\qquad\qquad \xi < -\dfrac{L}{2}, \\ Y_3(\xi) = \dfrac{\gamma}{2}\left[2 - \mathrm{e}^{-(L/2+\xi)}\cos(L/2 + \xi) \right. \\ \qquad \left. - \mathrm{e}^{-(L/2-\xi)}\cos(L/2 - \xi)\right], \\ \qquad\qquad -\dfrac{L}{2} \le \xi \le \dfrac{L}{2}. \end{cases} \quad (18)$$

It is noticed that in Figure 2, the beam static deflection is symmetric and the other two dynamic deflections (or wave shapes) are asymmetric. For both $\theta = 1$ and $\theta = 2$, the wave numbers of the front waves ($\xi > L/2 \approx 0$) are larger than those of the rear waves of $\xi < -L/2 \approx 0$, or say, the wavelengths of the front waves are smaller than those of the rear waves. As seen in eq. (14), the wave numbers of the front and rear waves are b_2 and b_1, respectively. The difference between b_2 and b_1 is their last term of $2\theta\beta/a$. Because θ and β are non-negative, $b_2 \geq b_1$. As shown later, the exponent of a decreases monotonically as the moving velocity of θ increases. As a result, the difference between b_2 and b_1 enlarges as θ increases, which then leads to a larger asymmetry in their wave shapes. While, it is also noticed that $\theta = 1$ is with the largest amplitude. The reason is that $\theta = 1$ is the critical velocity and thus the resonance point of the undamped system of a beam on an elastic foundation [12]. The resonance point of the damped system with $\beta = 0.1$ slightly shifts to a θ value smaller than 1. Compared with $\theta = 0$ and 2, $\theta = 1$ is closest to the resonance point and therefore, it has the largest amplitude. Besides the moving velocity θ, damping also plays an important role of determining the asymmetry. Chen and Chen [37] concluded that damping is the (only) mechanism responsible for the symmetry-breaking. When $\beta = 0$ and $\theta < 1$, $b_1 = b_2$ and the symmetry is thus reserved no matter what the moving speed is. While, $\theta = 0$ can also lead to $b_1 = b_2$. Furthermore, the Kenney's approximate analytical solution shows that even with $\beta = 0$, b_1 and b_2 will bifurcate into two different values when θ reaches the critical velocity and becomes supercritical [12]. Mathematically, the asymmetry is determined by the $2\theta\beta/a$ term as seen in eq. (14) and a is a function of θ and β. It is safe to conclude that the moving velocity and damping determine the asymmetry together rather than the damping alone.
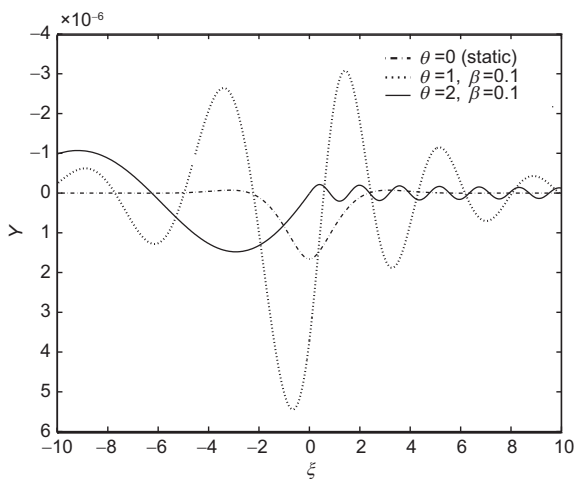
As shown in Figure 2, one characteristic of the asymmetry is that most of the beam deflection occurs behind the load. Physically, this is caused by that the energy of the deformation in the beam/foundation system propagates with an average velocity (considering all waves with different wavelengths) lower than that of the moving load [11]. It is also noticed that due to the presence of damping, the maximum beam displacement is no longer at the point of $\xi = 0$, but a point behind. As L approaches zero, the distributed mass model becomes a concentrated one [23]. Although the effect of distributed mass is mathematically indicated by α in eq. (10), our above results recover those of a moving concentrated load [12] as if only the load effect (γ) is present. Therefore, it confirms again that the concentrated mass has no impact on the critical velocity [18-20]. Furthermore, Frýba [31] proved that for the steady-state of an infinite beam traversed by a moving concentrated mass, the mass exerts no inertia effects. This is the mechanism why our wave shapes (with extremely small L) are the same as Kenney's [12] .

Figures 3 and 4 plot the beam wave shapes at the subcritical velocity of $\theta = 0.2$ for $\alpha = 5$ and $\alpha = 10$, respectively. The length of the distributed mass is fixed as $L = 180$ unless we specify otherwise. Here $L = 180$ physically corresponds to a realistic train length of $l = L/\lambda \approx 200$ m. As for a high-speed railway, its damping may vary in a large range of $0 < \beta < 0.8$ [36]. In Figures 3 and 4, three damping values of $\beta = 10^{-3}$, 0.2 and 0.8 are taken and the static deflection as given by eq. (18) is also plotted for comparison. For both $\alpha = 5$ and $\alpha = 10$ at this low subcritical velocity of $\theta = 0.2$, their differences between the wave shape and corresponding static deflections are very little. Their largest differences are in the transition area of Y_3 to Y_1, which are zoomed in for a closer examination. The deflections of all $\theta = 0.2$ are larger than their corresponding static deflections. As seen in eq. (10), due to the moving of the distributed mass, an effective axial compression of $4(1 + \alpha)\theta^2$ is exerted in the area of $-L/2 \leq \xi \leq L/2$ and an effective axial compression of $4\theta^2$ is exerted in the areas of $\xi > L/2$ and $\xi < -L/2$. The presence of these effective compressions reduces the system stiffness and thus lead to a larger deflection. For all $\theta = 0.2$ cases in Figures 3 and 4, their deflections monotonically decrease with the increase of damping (β).

Figures 5 and 6 plot the beam wave shapes at $\theta = 0.8$ for $\alpha = 5$ and $\alpha = 10$, respectively. As defined in eq. (9), $\theta_{cr2} = 0.4082$ and 0.3015 for $\alpha = 5$ and 10, respectively. This $\theta = 0.8$ value exceeds these two θ_{cr2}s. This $\theta = 0.8$ is a supercritical velocity in the distributed mass area but a subcritical one in other areas and therefore, we call it the transcritical velocity. As seen in Figures 5(a) and 6(a), the wave shapes are (almost) symmetric to $\xi = 0$ and with one dominant wave number (d_1) for very small damping of $\beta = 10^{-3}$.
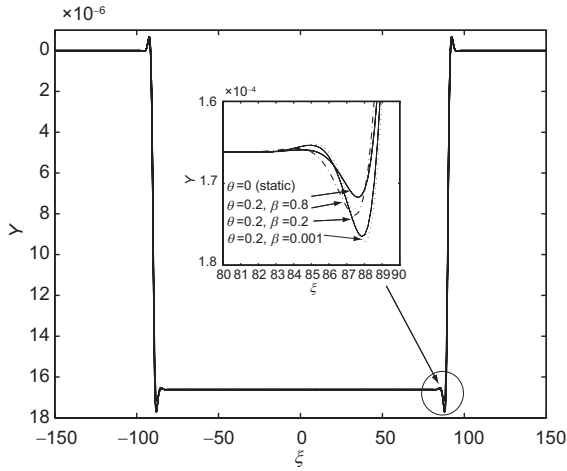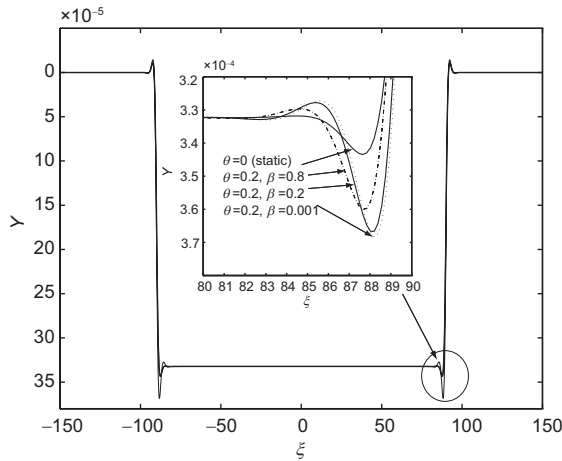

Figure 2   The moving mass is with $\alpha = 50$ and $L = 2 \times 10^{-3}$, which is used to simulate the concentrated load scenario. With the damping fixed as $\beta = 0.1$, three cases of $\theta = 0$, 1 and 2 are presented.

Figure 3   The wave shapes with $\alpha = 5$ at the subcritical velocity of $\theta = 0.2$ as compared with the corresponding beam static deformation. Here $L = 180$ and $\phi = 0$.


Figure 4   The wave shapes with $\alpha = 10$ at the subcritical velocity of $\theta = 0.2$ as compared with the corresponding beam static deformation. Here $L = 180$ and $\phi = 0$.

With $\theta = 0.8$ and $\beta = 10^{-3}$, the wavenumbers are $d_1 = 0.5148$ and $d_2 = 3.8852$. The corresponding wavelengths are $\lambda_{d1} = 2\pi/d_1 = 12.2055$ and $\lambda_{d2} = 2\pi/d_2 = 1.6172$ for $\alpha = 5$; and $d_1 = 0.3778$, $d_2 = 5.2931$ and $\lambda_{d1} = 2\pi/d_1 = 16.6283$, $\lambda_{d2} = 2\pi/d_2 = 1.187$ for $\alpha = 10$. The moving velocity (θ) and distributed mass (α) have much larger influence on the wave numbers than the damping. As β changes from 10^{-3} to 0.8, the wave numbers vary slightly. With the presence of the larger damping of $\beta = 0.2$ and 0.8, the waves become asymmetric: the waves with the wave number of d_2 cluster on the left and the waves with d_1 cluster on the right. As seen in both Figures 5 and 6, the wave amplitudes monotonically decrease and the asymmetry becomes more outstanding with the increase of damping. Compared with that in Figures 3 and 4, the damping in Figures 5 and 6 with a higher moving velocity has much more pronounced influence on the deflection amplitude, which is also noticed by Achenbach and Sun [30].
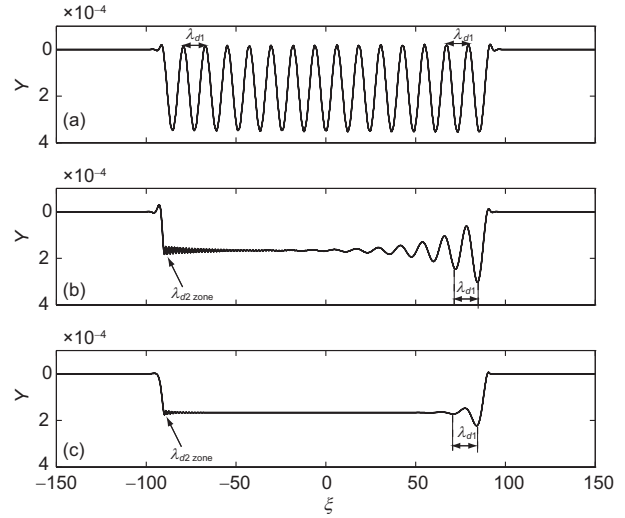
Figure 5   The wave shapes with $\alpha = 5$ at $\theta = 0.8$ with different dampings. (a) $\beta = 10^{-3}$: The wave numbers are $d_1 = 0.5148$ and $d_2 = 3.8852$; the corresponding wavelengths are $\lambda_{d1} = 2\pi/d_1 = 12.2055$ and $\lambda_{d2} = 2\pi/d_2 = 1.6172$. (b) $\beta = 0.2$: The wave numbers are $d_1 = 0.5128$ and $d_2 = 3.886$; the corresponding wavelengths are $\lambda_{d1} = 12.2516$ and $\lambda_{d2} = 1.6168$. (c) $\beta = 0.8$: The wave numbers are $d_1 = 0.4833$ and $d_2 = 3.8968$; the corresponding wavelengths are $\lambda_{d1} = 12.8663$ and $\lambda_{d2} = 1.6123$. Here $L = 180$ and $\phi = 0$.
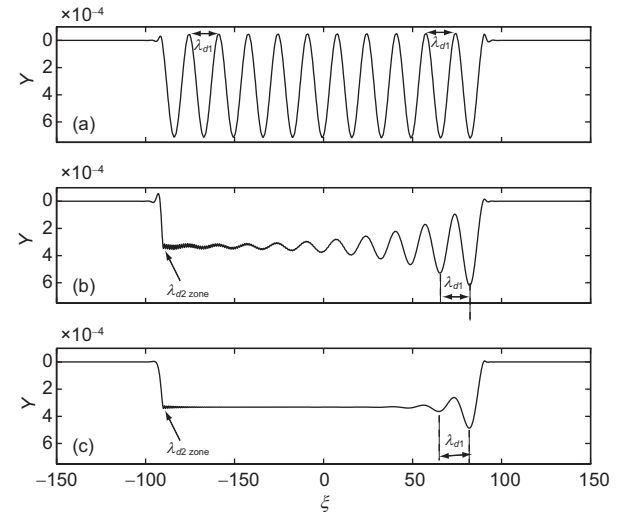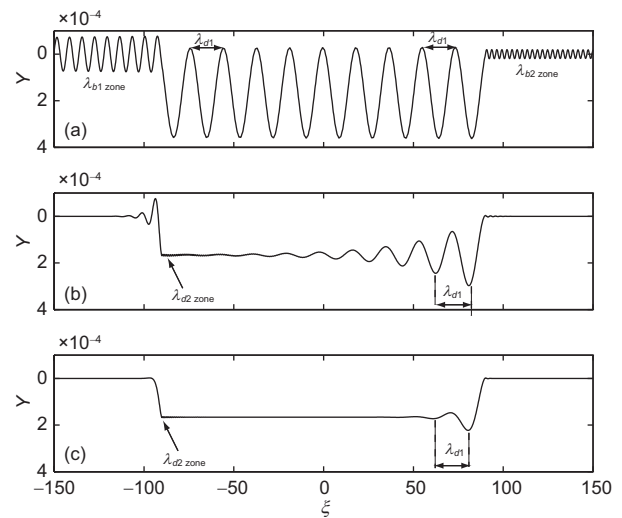

Figure 6   The wave shapes with $\alpha = 10$ at $\theta = 0.8$ with different dampings. (a) $\beta = 10^{-3}$: The wave numbers are $d_1 = 0.3778$ and $d_2 = 5.2931$; the corresponding wavelengths are $\lambda_{d1} = 2\pi/d_1 = 16.6283$ and $\lambda_{d2} = 2\pi/d_2 = 1.187$. (b) $\beta = 0.2$: The wave numbers are $d_1 = 0.3771$ and $d_2 = 5.2933$; the corresponding wavelengths are $\lambda_{d1} = 16.6598$ and $\lambda_{d2} = 1.187$. (c) $\beta = 0.8$: The wave numbers are $d_1 = 0.3663$ and $d_2 = 5.2955$; the corresponding wavelengths are $\lambda_{d1} = 17.1522$ and $\lambda_{d2} = 1.1865$. Here $L = 180$ and $\phi = 0$.

Compared with the asymmetry pattern in Figure 2, there is a fundamental difference in Figures 5 and 6. As mentioned above, in Figure 2 shorter wave is ahead of concentrated load and the longer wave is behind. In contrast, things are reversed in the distributed mass area of $-L/2 \leq \xi \leq L/2$ as seen in Figures 5 and 6: shorter wave is now behind in the

area of $-L/2 \leq \xi \leq 0$ and longer wave is ahead in the area of $0 \leq \xi \leq L/2$. For the concentrated load case, as $L \to 0$, the wave is described by $Y_1(\xi) = \mathrm{e}^{-a\xi}[C_1 \sin(b_2\xi) + C_2 \cos(b_2\xi)]$ for $\xi > 0$ and $Y_2(\xi) = \mathrm{e}^{a\xi}[C_3 \sin(b_1\xi) + C_4 \cos(b_1\xi)]$ for $\xi < 0$ only. The wave numbers as described by eq. (14) show $b_2 > b_1$ with the presence of damping, which is the mechanism for the asymmetry of the moving concentrated load problem. While, for the distributed mass problem, L is long and the asymmetry actually arises in the three areas of $\xi < -L/2$, $-L/2 \leq \xi \leq L/2$ and $\xi > L/2$. The asymmetry pattern of the concentrated load is still followed in the two areas outside the distributed mass: the shorter wave with a large wave number is ahead in the $\xi > L/2$ area and the longer wave with a small wave number is behind in the $\xi < -L/2$ area. However, their amplitudes are very small as compared with those in the distributed mass area. In the distributed mass area of $-L/2 \leq \xi \leq L/2$, the wave is described by $Y_3(\xi) = \mathrm{e}^{-c\xi}[C_5 \sin(d_2\xi) + C_6 \cos(d_2\xi)] + \mathrm{e}^{c\xi}[C_7 \sin(d_1\xi) + C_8 \cos(d_1\xi)]$. As the exponent c is a positive number, $\mathrm{e}^{-c\xi}[C_5 \sin(d_2\xi) + C_6 \cos(d_2\xi)]$ is the dominant term in the area of $-L/2 \leq \xi \leq 0$ and $\mathrm{e}^{c\xi}[C_7 \sin(d_1\xi) + C_8 \cos(d_1\xi)]$ is the dominant one in the area of $0 \leq \xi \leq L/2$. The wave numbers of d_1 and d_2 are given in eq. (14) and $d_2 > d_1$, which is the reason for the reversal asymmetry pattern in the $-L/2 \leq \xi \leq L/2$ area of distributed mass. When Figures 5(b) and 6(b) are compared, a rather significant difference is noticed: The wave shape in Figure 5(b) is rather flat around $\xi = 0$ and in contrast, the corresponding one in Figure 6(b) oscillates significantly. The magnitude difference can be explained by different αs, which result in different transverse loads of γs. The mechanism for the wave shape difference, or say, the asymmetry, needs to be addressed. As discussed above, we conclude that θ and β are the combined mechanism responsible for the asymmetry of wave shapes for the concentrated load case. Similarly, the difference between d_1 and d_2 is their last term of $2\theta\beta/c$ and the exponent c is determined by eq. (13), in which the axial load ϕ and distributed mass α both play a role. In summary, for the moving distributed mass problem, there are four factors determining the wave shape/asymmetry: moving velocity, damping, axial load and distributed mass. Here the wave shape difference between Figures 5(b) and 6(b) results from the distributed mass of α.

Figures 7 and 8 plot the beam wave shapes at $\theta = 1.2$ for $\alpha = 5$ and $\alpha = 10$, respectively. This $\theta = 1.2$ value exceeds $\theta_{cr1} = 1$, which is the supercritical case. In Figures 7 and 8, the symmetric and asymmetric patterns inside the distributed mass area of $-L/2 \leq \xi \leq L/2$ follow the same trends as those in Figures 5 and 6. The main pattern differences between the waves with $\theta > 1$ (supercritical) and the waves with $\theta_{cr2} < \theta < \theta_{cr1} = 1$ (transcritical) are in the areas of $\xi < -L/2$ and $\xi > L/2$, especially when β is small. These

differences are most outstanding in Figures 7(a) and 8(a): The wave with a large wave number of b_2 (or a small wavelength of λ_{b2}) arises in the $\xi > L/2$ area; the wave with a small wave number of b_1 (or a large wavelength of λ_{b1}) arises in the $\xi < -L/2$ area. Their wave amplitudes are also significant. Actually, if $\beta = 0$, the waves with the b_2 and b_1 wave numbers will extend to $\pm\infty$ without any decay, which implies infinite energy. Although the axially moving mechanical system is non-conservative [38], this kind of wave shape configuration raises the concern that it might violate

Figure 7   The wave shapes with $\alpha = 5$ at the supercritical velocity $\theta = 1.2$ with different dampings. (a) $\beta = 10^{-3}$: The wave numbers are $b_1 = 0.8987$, $b_2 = 2.2253$, $d_1 = 0.3408$ and $d_2 = 5.8689$; the corresponding wavelengths are $\lambda_{b1} = 6.9912$, $\lambda_{b2} = 2.8234$, $\lambda_{d1} = 18.437$ and $\lambda_{d2} = 1.0705$. (b) $\beta = 0.2$ and (c) $\beta = 0.8$. Here $L = 180$ and $\phi = 0$.
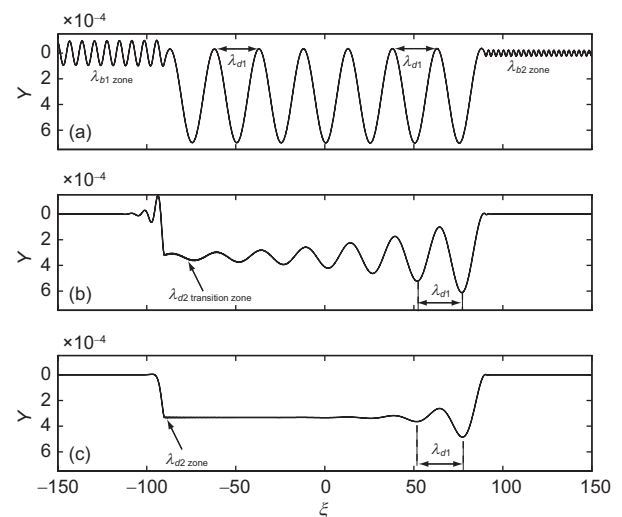

Figure 8   The wave shapes with $\alpha = 10$ at the supercritical velocity $\theta = 1.2$ with different dampings. (a) $\beta = 10^{-3}$: The wave numbers are $b_1 = 0.8987$, $b_2 = 2.2254$, $d_1 = 0.25137$ and $d_2 = 7.9559$; the corresponding wavelengths are $\lambda_{b1} = 6.9912$, $\lambda_{b2} = 2.8234$, $\lambda_{d1} = 24.995$ and $\lambda_{d2} = 0.7897$. (b) $\beta = 0.2$ and (c) $\beta = 0.8$. Here $L = 180$ and $\phi = 0$.

the energy conditions because of this infinite energy. For a moving concentrated load problem, Kenney argued that such wave configuration can be achieved without any energy violation [12]. In contrast, for a moving concentrated mass problem, Metrikine and Dieterman [19] said that such steady state can never be reached.

Figures 3 to 8 present the wave shapes in three moving velocity zones: $\theta < \theta_{cr2}$ (subcritical), $\theta_{cr2} < \theta < \theta_{cr1} = 1$ (transcritical) and $\theta > 1$ (supercritical). In these three velocity zones, there are qualitative differences of wave shapes: in the subcritical region, there is only a small deviation of the wave shapes from the static deflection; in the transcritical region, the waves are still mostly trapped in the distributed mass area but their shapes are significantly different from a static one; in the supercritical region, the wave shapes in the distributed mass area are similar to those of the transcritical region, but now shorter waves propagate ahead of the distributed mass area and longer waves are left behind. A similar scenario is encountered in a Timoshenko beam on an elastic foundation under a moving concentrated load, in which there are three critical velocities, and the wave shapes are also qualitatively different as the load moving velocity is in the different zones as demarcated by these three critical velocities [30]. To explain the differences of wave shapes in the three velocity zones, we need to examine how the wave numbers and exponents vary with the moving velocity, which are presented in Figures 9 and 10 for $\alpha = 5$ and 10. Figures 9(a) and (b) plot the wave numbers and exponents of $\alpha = 5$, respectively. For $\beta = 10^{-3}$ (close to zero), $\theta_{cr2} = \sqrt{1/(1 + \alpha)} = 0.4082$ and $\theta_{cr1} = 1$. In Figure 9, one wave number bifurcates into two of d_1 and d_2 at $\theta = \theta_{cr2} = 0.4082$, which is marked by a solid circle; the exponent c becomes zero at and remains zero afterwards. Similarly, one wave number bifurcates into two of b_1 and b_2 at $\theta = 1$, which is also marked by a solid circle; the exponent a becomes zero at and remains zero afterwards. As seen in eq. (15), the waves decay exponentially with the rate of $e^{-|c\xi|}$ in $-L/2 \leq \xi \leq L/2$ and the rate of $e^{-|a\xi|}$ in $\xi < -L/2$ and $\xi > L/2$. At $\theta = 0.2$, both a and c are significantly large. As a result, the waves decay rapidly inside and outside the distributed mass areas and only the static deformation is left, which is the reason why the waves in Figures 3 and 4 resemble a static deflection. At $\theta = 0.8$, a is still significantly large and $c = 0$. With $c = 0$ and thus no decay, the waves inside the $-L/2 \leq \xi \leq L/2$ area of distributed mass are now "activated". While, the waves outside $-L/2 \leq \xi \leq L/2$ still experience severe decay due to a large a and thus remain "inactivated", which is the results as seen in Figure 5(a). At $\theta = 1.2$, both $a = 0$ and $c = 0$, the waves are now "activated" in all areas, which is seen in Figure 7(a). With a larger damping of $\beta = 0.2$, the exponents of a and c are significantly larger than those with $\beta = 10^{-3}$ as seen in Figure 9(b): c of

$\beta = 0.2$ slows down its decrease rather than plunging into zero as that of $\beta = 10^{-3}$. Larger damping results in larger
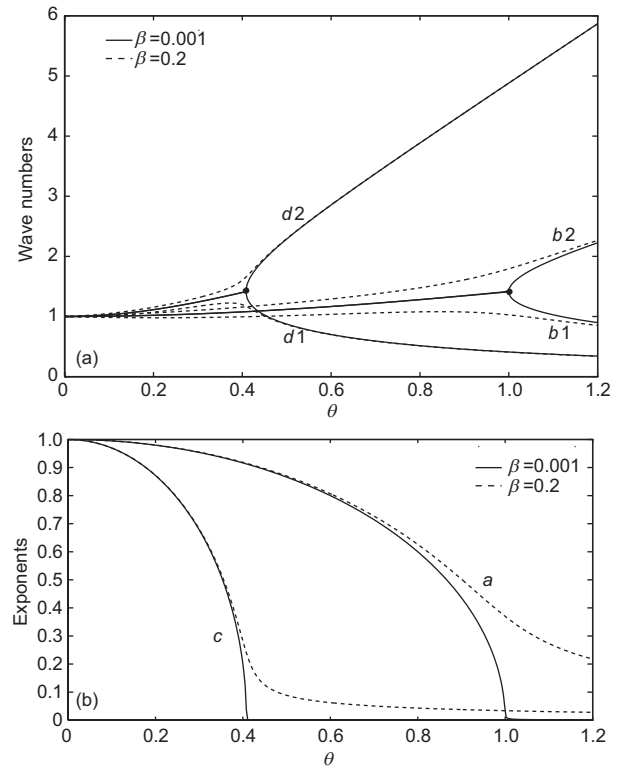
Figure 9 (a) The wave numbers and (b) exponents of $\alpha = 5$ as the functions of the moving velocity with $\beta = 10^{-3}$ and $\beta = 0.2$, respectively.
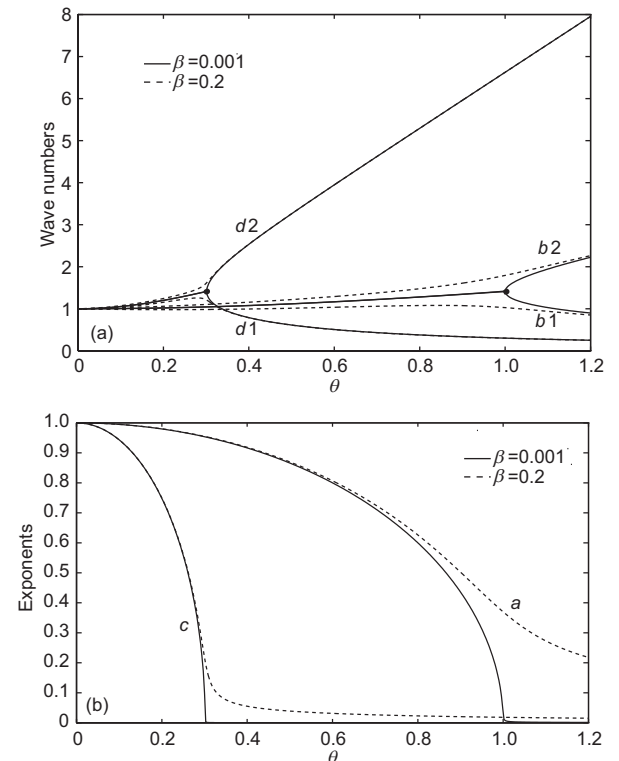
Figure 10 (a) The wave numbers and (b) exponents of $\alpha = 10$ as the functions of the moving velocity with $\beta = 10^{-3}$ and $\beta = 0.2$, respectively.

exponents of a and c, which leads to more severe wave decay both inside and outside the distributed mass area. Furthermore, as seen in Figure 9(a), larger damping also makes the wave numbers of b_1 and d_1 smaller and those of b_2 and d_2 larger. Strictly speaking, with the presence of damping there is no wave number bifurcation: The wave numbers begin to separate from each other as far as $\theta > 0$, which can be seen in both Figure 9(a) and eq. (14). Figures 10(a) and (b) plot the wave numbers and exponents of $\alpha = 10$. The difference is that θ_{cr2} becomes smaller as $\sqrt{1/(1+\alpha)} = 0.3015$. The above analyses can still be applied to explain the wave pattern variations in Figures 4, 6 and 7. Here we need to address an issue why we use $\beta = 10^{-3}$ rather than directly computing the $\beta = 0$ case. In eq. (14), the last term of b_1 and b_2 is $2\theta\beta/a$. When $\beta = 0$, the solution of $a = [1 - (\phi + \theta^2)^2]^{1/2}$ is found from eq. (12). Therefore, as $\phi = 0$ and $\theta = 1$, the $\frac{0}{0}$ type of problem is encountered when calculating $2\theta\beta/a$. The same thing occurs for the $2\theta\beta/c$ term in d_1 and d_2 as $\theta = \theta_{cr2}$. The computer cannot carry out such $\frac{0}{0}$ type of calculation without further manipulation and therefore, instead of $\beta = 0$, the computation of $\beta = 10^{-3}$ is carried out for the simplicity reason.

All our above discussions only show the roles of wave numbers and exponents, which are all independent of the length of the distributed mass. The length L actually only appears in the boundary conditions of eqs. (16) and (17). Figure 2 examines a special case of concentrated load and mass by setting very small valuse for L. Now we study the length effect in more details. Figure 11 plots the wave shapes of $L = 120$ and $L = 180$ with the same $\alpha = 5$, $\theta = 0.8$ and $\beta = 0.2$ to see how L impacts the wave shapes. The wave shape of $L = 180$ is also presented in Figure 5(b). As both share the same wave numbers and exponents, the related discussion on the wave shape asymmetry of $L = 180$ still applies to that of $L = 120$: The wave with the wave number of d_2 clusters on the left side and the wave with wave number of d_1 clusters on the right side. As seen in Figure 11, the maximum displacements of $L = 120$ and 180 are the same; their wave shapes outside the distributed mass area are also the same. Their major shape differences are around in the center. Those coefficients of C_is in eqs. (15) vary with different L, which is mathematically responsible for the wave shape difference. Physically, the length of the distributed mass gives the space in which the waves with the given wave numbers and exponents have to accommodate their shapes. As seen in the right side of Figure 11, the two waves with the two different Ls are (almost) in the opposite phases.

Figures 3 to 8 provide a comparative study of the waves with two different distributed masses. Figure 12 provides a more succinct summary of their differences. As seen in Figure 11, the beam maximum displacements appear on the right

side of the distributed mass area. The maximum displacement, which is one of the most important characteristics in the wave shapes, is selected as the parameter in Figure 12 to study the effect of α. In Figure 12, the maximum displacements of $\alpha = 5$ and 10 as the functions of moving velocity are presented. For each α value, eight branches with different dampings ranging from $\beta = 0.1$ to 0.8 are plotted. It is seen that for both $\alpha = 5$ and 10, the maximum displacements monotonically decrease with the increase of β because larger damping dissipates more energy. The maximum displacement of $\alpha = 5$ is always smaller than that of $\alpha = 10$. Larger α results in both a larger transverse (γ) and an axially compressive $((1+\alpha)\theta^2\partial^2 Y/\partial\xi^2)$ loads. Larger axial load leads to smaller stiffness. Therefore, in conjunction with a larger transverse load and a smaller stiffness, larger α always results in a larger maximum displacement. Actually, besides the maximum displacement, at any given point of ξ,
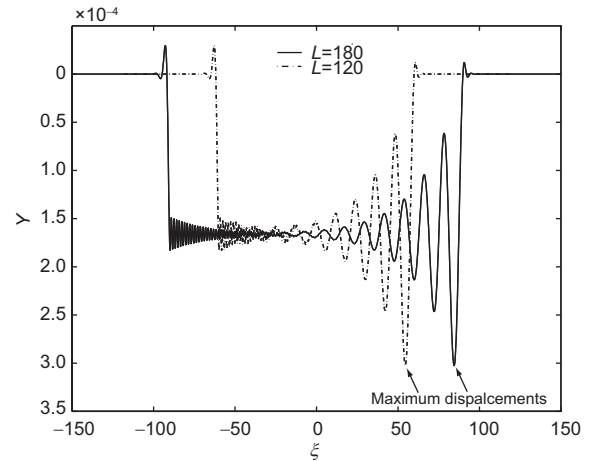

Figure 11   The wave shapes of $L = 120$ and $L = 180$ with $\alpha = 5$, $\theta = 0.8$ and $\beta = 0.2$. Here $\phi = 0$.
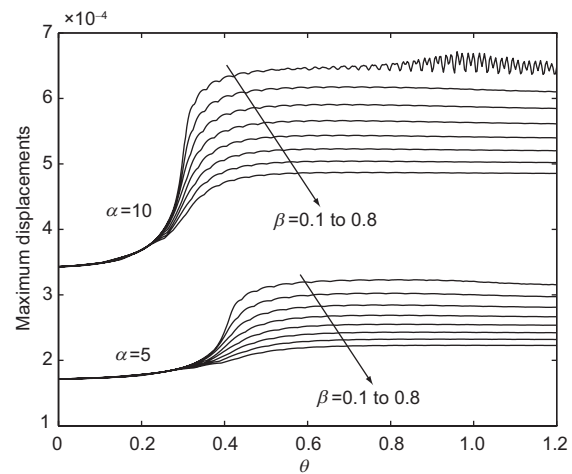

Figure 12   The maximum displacements of $\alpha = 5$ and $\alpha = 10$ as the functions of the moving velocity θ. For each α, there are eight different dampings ranging from $\beta = 0.1$ to 0.8. Here $L = 180$ and $\phi = 0$.

the displacement with a larger α is always larger, which can be clearly seen in Figures 3 to 8. In Figure 12, it is noticed that at a low moving velocity, for each α the eight branches stick together. Their separation starts around θ_{cr2}. For $\alpha = 5$ and $\alpha = 10$, the corresponding θ_{cr2}s are $\theta_{cr2} = 0.3015$ and $\theta_{cr2} = 0.4082$. Once those branches begin to separate, they experience a rapid increase and then reach a plateau. As given in eq. (15), the exponent c plays a vital role of determining the Y_3 wave amplitude. As seen in Figures 9(b) and 10(b): Around θ_{cr2}, the exponent c experiences a rapid decrease, then its decrease rate is dramatically slowed down and finally maintains as small constant. This c exponent variation pattern is responsible for the rapid increase and then keeping flat behavior of the maximum displacements in Figure 12. Similarly, around $\theta_{cr1} = 1$, the exponent a also experiences a rapid decrease. While, this a exponent is associated with the Y_1 and Y_2 wave amplitudes outside the distributed mass area, which has no impact the Y_3 wave. The a exponent influences on the Y_1 and Y_2 waves are seen in Figures 7 and 8.

Here we need to address an important issue on the "resonance". Kenney presented the plot of the wave amplitude versus the moving velocity of a concentrated load [12], which looks very similar to a frequency response plot. While, our Figure 12 looks completely different from Kenney's Figure 3 [12]. Kenney named $\theta_{cr1} = 1$ as the "point of resonance" [12], at which the wave amplitude with $\beta = 0$ becomes infinitely large. However, Mathews [34] argued that this is purely a velocity effect; and as there is no periodic force involved, it cannot be described as a resonance. This "resonance" associated with the critical velocity of $\theta_{cr1} = 1$ is preferred as an analogy to the sonic boom [34]. According to Metrikine and Dieterman [19], this "resonance" is caused by an anomalous Doppler effect, which intensifies the vibration of a certain part of beam by transferring the energy from other parts. Physically, this "resonance" can also be interpreted by two different mechanisms. One is the buckling or more generally speaking, zero effective stiffness. As the concentrated load moving velocity reaches the critical velocity of $\theta_{cr1} = 1$, it generates an effective axial compression equal to the static buckling load for an infinite beam on an elastic foundation [3]. As for the moving string case, the critical velocity is defined as the effective string tension becomes zero [39], which also corresponds to the zero effective stiffness of a string. The other is that the cut-off frequency becomes zero [20]. For a vibrating beam on an elastic foundation, there are three different solution forms of the mode shapes depending on whether the beam vibrating frequency is larger, lower or equal to the cut-off frequency [40, 41]. When the vibrating frequency is equal to this cut-off frequency, there is no spatial variation in the beam motions, or say, vibration; only rigid body motion exists [40, 41]. Simi-

larly, at the critical velocity, there are no reflected waves for a standing wave of the string vibration because the string axially moving speed is larger than the wave speed [39]. Kenney's system is an infinite beam on an elastic foundation under a moving concentrated load [12]. In comparison, our system consists of three parts: A finite beam section with a moving distributed mass and two semi-infinite beam sections. As defined in eqs. (7) and (8), $\theta_{cr2} = \sqrt{1/(1+\alpha)}$ is the critical velocity for an infinite beam with the $1 + \alpha$ mass per unit length. Therefore, θ_{cr2} is not a "resonance point" for either the finite beam section with the distributed mass or the two semi-infinite beams. Similarly, as the finite beam section with the distributed mass divides an infinite beam into two semi-infinite beams, $\theta_{cr1} = 1$ is not a "resonance point" for the Y_1 and Y_2, either. A similar scenario also occurs in the problem of a beam on an elastic foundation under a moving distributed load: there is no "resonance" and the beam motion is bounded in time [42].

In Figures 2 to 12, the axial load of ϕ is set to be zero. The effects of the axial load are now examined in Figures 13-15. With the presence of axial load, the critical velocities becomes the following [3]:

$$\frac{v_{acr1}^2}{v_{cr1}^2} + \frac{N}{N_{cr}} = 1, \quad \frac{v_{acr2}^2}{v_{cr2}^2} + \frac{N}{N_{cr}} = 1, \tag{19}$$

where v_{cr1} and v_{cr2} are the two critical velocities defined in eq. (7) for the zero axial cases; v_{acr1} and v_{acr2} are the two corresponding critical velocities with the presence of the axial load N. Here N_{cr} also defined in eq. (7) is the beam buckling load. The above equations can also be written as the following dimensionless forms:

$$\theta_{acr1}^2 + \phi = 1, \quad \frac{\theta_{acr2}^2}{\theta_{cr2}^2} + \phi = (1+\alpha)\theta_{acr2}^2 + \phi = 1. \tag{20}$$

From the above equations, the critical velocities with the presence of an axial load are solved as $\theta_{acr1} = \sqrt{1-\phi}$ and $\theta_{acr2} = \sqrt{(1-\phi)/(1+\alpha)}$. Clearly, compression (positive ϕ) decreases the critical velocities and tension (negative ϕ) increases them. For $\phi = 0.5$, 0 and -0.5, the corresponding critical velocities are $\theta_{acr1} = 0.7071$, 1, 1.2247 and $\theta_{acr2} = 0.2132$, 0.3015, 0.3693, respectively. Here the $\phi = 0$ case is presented in Figure 10. The other two cases of $\phi = 0.5$ and -0.5 show the same pattern behaviors as seen in Figures 13 and 14: The wave numbers d_1 and d_2 bifurcate at their corresponding θ_{acr2}s and the exponent c associated with these two wave numbers experiences a rapid decrease approaching zero; the wave numbers b_1 and b_2 bifurcate at their corresponding θ_{acr1}s and the exponent a associated with these two wave numbers experiences a rapid decrease approaching zero. The presence of an axial load together with the distributed mass changes the two critical velocities. As a result,

the wave numbers and exponents, which directly determine the wave shapes, are also changed. In comparison, the distributed mass can only change one critical velocity of θ_{cr2}. As seen in Figure 13, before the bifurcations a smaller ϕ results in smaller wave numbers with a given θ; after the bifurcations, a smaller ϕ results in smaller b_2, d_2 and larger b_1, d_1. As seen in Figure 14, a smaller ϕ always results in larger exponents of a and c.

Here an additional benefit of the axial load modeling is worthy to be addressed. As the Winkler foundation model is used in this study and physically, it is to model the supporting elastic continuum as a spring layer. To more accurately capture the deformation of an elastic continuum, various foundation models are developed by adding more layers to the spring layer. For example, the Filonenko-Borodich foundation is a spring layer plus a membrane layer; the Pasternak foundation is a spring layer plus a shear layer [43]. The
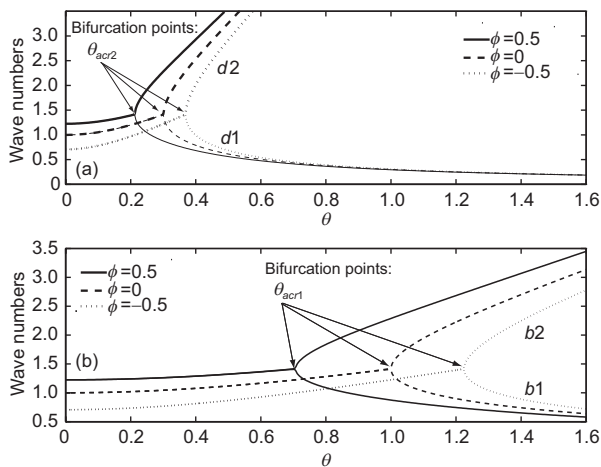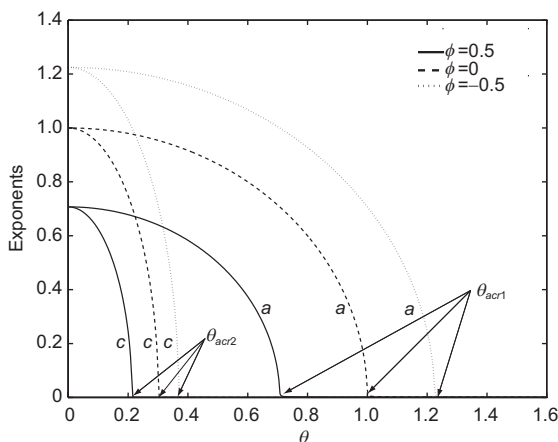
essential improvement of the above two foundation models is that the independent Winkler springs are now connected by a membrane/shear layer and interact to one another [44, 45], which better characterizes an elastic continuum. Because one more layer is added, an additional parameter is needed to characterize the layer besides the spring stiffness: the membrane tension for the Filonenko-Borodich foundation and the shear layer constant for the Pasternak foundation, which is the so-called two-parameter foundation model. These two-parameter foundation models are mathematically equivalent to the Winkler foundation model with the presence of a tensile axial load [44, 45]. Therefore, our model of eq. (1) can also be used to describe the two-parameter foundation by simply modifying the axial load of N.

As discussed above, the two critical velocities are the vital parameters to determine the wave numbers and exponents. As given in eq. (20), these two critical velocities are plotted in Figure 15 as the functions of ϕ and θ. Both θ_{acr1} and θ_{acr2} increase monotonically with the decrease of ϕ. At $\phi = 1$ of the buckling load, both velocities become zero. Because $\theta_{acr1} = \sqrt{1-\phi}$ is independent of α, it is parallel to the α-axis; $\theta_{acr2} = \sqrt{(1-\phi)/(1+\alpha)}$ leads to its monotonic decrease with α. Clearly, larger ϕ and α result in two smaller critical velocities. As seen in Figure 14, smaller critical velocities also result in smaller exponents of a and c. As the exponents determine the wave amplitude decaying rates, smaller exponents mean smaller decaying rates and thus larger amplitudes. Therefore, besides the earlier conclusion of tension (negative ϕ) improving the critical velocities [3], tension also reduces the wave amplitudes.

In our model, there are two implicit assumptions. One is that the moving distributed mass is firmly attached to the beam, i.e., there is no separation between mass and beam [46]. In the moving train dynamics, this separation phenomenon is referred to as "jumping wheel" [5, 6], which often occurs when there is a sudden stiffness change of the beam/foundation. Furthermore, our distributed load is a uniform one due to the gravity, which implies that the mass and

Figure 13   The wave numbers as the functions of the moving velocity θ when $\phi = -0.5$, 0 and = 0.5 with $\alpha = 10$ and $\beta = 10^{-3}$. (a) The d_1 and d_2 branches. (b) The b_1 and b_2 branches. Here $L = 180$.
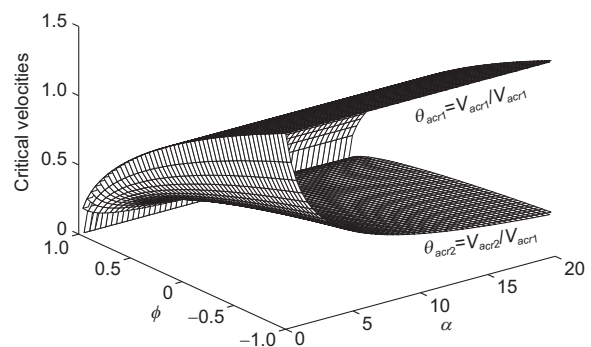

Figure 14   The exponents as the functions of the moving velocity θ when $\phi = -0.5$, 0 and = 0.5 with $\alpha = 10$ and $\beta = 10^{-3}$. Here $L = 180$.

Figure 15   The two critical velocities as the functions of ϕ and α. The upper one is $\theta_{acr1} = v_{acr1}/v_{cr1}$ and the lower one is $\theta_{acr2} = v_{acr2}/v_{cr1}$.

beam form a *de facto* line contact [47]. The other is that the Winkler foundation response to compression and tension is the same. As seen in Figures 5(a) to 8(a), some of the beam displacements become negative because of large wave amplitudes. The negative displacement means that the beam bends upwards, which causes tension inside the elastic foundation. In a realistic railway system, the elastic foundation modulus (k) is often with two different values in its response to tension and compression, which is the so-called bilinear model [48]. The extreme scenario is that $k = 0$ in response to tension and the elastic foundation is thus referred to as the tensionless foundation [35, 37], which is often used to study the ballasted railway track/support responses. In our model, the same k applies for both tension and compression. The tensionless foundation model is a nonlinear one due to the unknown property of the separation area(s) [35, 37, 48]. This asymmetric response of elastic foundation to tension and compression will be included in our future study to more realistically model the train/track response.

4   Conclusion

In the problem of a moving distributed mass and load, there are two critical velocities because of the moving mass effect. Due to the presence of the distributed mass and load, the space is divided into three domains. In these three domains, there are three different waves with four different wave numbers (b_1, b_2, d_1 and d_2) and two different exponents (a and c), which determine the wave shapes. The two critical velocities determine the variation patterns of the wave numbers and exponents: the wave numbers bifurcate and the exponents rapidly approach zero at each critical velocity for the no damping case. Larger damping results in the large exponents of both a and c, which leads to the larger wave amplitude reduction both inside and outside the distributed mass area; larger damping makes some wave numbers (b_2 and d_2) larger and some (b_1 and d_1) smaller. As a result, these variation patterns of the wave numbers and exponents cause significant wave shape changes as the moving velocity varies. The moving velocity and damping play a major role in determining the symmetry/asymmetry of the wave shapes. The wave numbers and exponents are independent of the distributed mass length. The effect of the distributed mass length is to delimit a space to accommodate the waves with the given wave numbers and exponents; its major influence is on the wave shape around the center of the distributed mass and wave phase. Besides the moving velocity and damping, the distributed mass and axial load are the two other factors determining the wave numbers and exponents. A larger distributed mass reduces the lower critical velocity and thus one exponent of c, which

leads to a larger wave amplitude inside the distributed mass area. Axial load changes the two critical velocities at the same time: tension increases both and compression reduces both. Compared with the moving concentrated load problem, there is no "resonance" of the wave amplitude response to the moving velocity in the moving distributed mass and load problem.

1   S. P. Timoshenko, *Method of Analysis of Statical and Dynamical Stresses in Rail* (Proceedings of the Second International Congress for Applied Mechanics, Zurich, Switzerland, 1926).
2   J. J. Labra, Acta Mech. **22**, 113 (1975).
3   A. D. Kerr, Int. J. Mech. Sci. **14**, 71 (1972).
4   S. P. Timoshenko, and B. F. Langer, J. Appl. Mech. **54**, 277 (1932).
5   M. T. Tran, K. K. Ang, and V. H. Luong, J. Sound Vib. **333**, 5427 (2014).
6   K. K. Ang, and J. Dai, J. Sound Vib. **332**, 2954 (2013).
7   N. H. Lim, N. H. Park, and Y. J. Kang, Comput. Struct. **81**, 2219 (2003).
8   A. V. Metrikine, and H. A. Dieterman, Eur. J. Mech. A-Solids **16**, 295 (1997).
9   Y. G. Chen, and B. Jin, Sci. China Ser. G-Phys. Mech. Astron. **51**, 883 (2008).
10   B. Jin, Archive Appl. Mech. **74**, 277 (2004).
11   A. K. Mallik, S. Chandra, and A. B. Singh, J. Sound Vib. **291**, 1148 (2006).
12   J. T. Kenney, J. Appl. Mech. **21**, 359 (1954).
13   Z. Dimitrovová, and J. N. Varandas, Comput. Struct. **87**, 1224 (2009).
14   Z. Dimitrovová, Int. J. Solids Struct. **122-123**, 128 (2017).
15   A. Nobili, J. Eng. Mech. **139**, 1470 (2013).
16   R. Bogacz, and W. Czyczula, J. Theor. Appl. Mech. **46**, 763 (2008).
17   A. V. Vostroukhov, and A. V. Metrikine, Int. J. Solids Struct. **40**, 5723 (2003).
18   D. G. Duffy, J. Appl. Mech. **57**, 66 (1990).
19   A. V. Metrikine, and H. A. Dieterman, J. Sound Vib. **201**, 567 (1997).
20   Z. Dimitrovová, Int. J. Mech. Sci. **127**, 142 (2017).
21   H. D. Nelson, and R. A. Conover, J. Appl. Mech. **38**, 1003 (1971).
22   G. A. Benedetti, J. Appl. Mech. **41**, 1069 (1974).
23   E. Esmailzadeh, and M. Ghorashi, J. Sound Vib. **184**, 9 (1995).
24   Y. H. Lin, J. Sound Vib. **199**, 697 (1997).
25   X. Bian, H. Jiang, C. Cheng, Y. Chen, R. Chen, and J. Jiang, Soil Dyn. Earthquake Eng. **66**, 368 (2014).
26   W. L. Luo, Y. Xia, and S. Weng, Sci. China-Phys. Mech. Astron. **58**, 084601 (2015).
27   K. D. Murphy, and Y. Zhang, J. Sound Vib. **237**, 319 (2000).
28   X. M. Zhou, and Y. C. Zhao, Sci. China-Phys. Mech. Astron. **62**, 014612 (2019).
29   J. H. Yang, Q. Z. Yuan, and Y. P. Zhao, Sci. China-Phys. Mech. Astron. **62**, 124611 (2019).
30   J. D. Achenbach, and C. T. Sun, Int. J. Solids Struct. **1**, 353 (1965).
31   L. Frýba, *Vibration of Solids and Structures under Moving Loads* (Noordhoff International Publishing, Groningen, Netherland, 1972).
32   M. A. Biot, J. Appl. Mech. **4**, 1 (1937).
33   M. Hetényi, *Beams on Elastic Foundation* (The University of Michigan Press, Ann Arbor, Michigan, USA, 1946).
34   P. M. Mathews, Z. Angew. Math. Mech. **38**, 105 (1958).

35 Y. Zhang, and K. D. Murphy, Int. J. Solids Struct. **41**, 6745 (2004).

36 Y. H. Chen, Y. H. Huang, and C. T. Sun, J. Sound Vibr. **241**, 809 (1997).

37 J. S. Chen, and Y. K. Chen, Int. J. Non-Linear Mech. **46**, 180 (2011).

38 B. Tabarrok, C. Tezer, and M. Stylianou, Acta Mech. **107**, 137 (1994).

39 C. Y. Wang, Acta Mech **228**, 357 (2017).

40 Y. Zhang, and K. D. Murphy, Acta Mech. Solid Sin. **20**, 236 (2007).

41 K. F. Graff, *Wave Motions in Elastic Solids* (Clarendon Press, Oxford, UK, 1975).

42 C. R. Steele, J. Appl. Mech. **35**, 481 (1968).

43 A. D. Kerr, J. Appl. Mech. **31**, 491 (1964).

44 Y. Zhang, and X. Liu, Eur. J. Mech. A-Solids **77**, 103819 (2019).

45 S. C. Dutta, and R. Roy, Comput. Struct. **80**, 1579 (2002).

46 U. Lee, J. Vib. Acoust. **118**, 516 (1996).

47 H. Zhu, Y. Zhao, Z. He, R. Zhang, and S. Ma, Sci. China-Phys. Mech. Astron. **61**, 054611 (2018).

48 Y. Zhang, X. Liu, and Y. Wei, Eur. J. Mech. A-Solids **71**, 394 (2018).

49 Y. Zhang, Sci. China-Phys. Mech. Astron. **59**, 624602 (2016).

50 G. A. Korn, and T. M. Korn, *Mathematical Handbook for Scientist and Engineers, 2nd ed.* (McGraw-Hill Book Company, New York, USA, 1968).

Appendix   Solutions to the governing equations of eq. (10)

To solve the governing equation, we firstly need to seek the homogeneous solutions. The homogeneous parts of eq. (10) are as follows:

$$
\begin{cases}
\dfrac{\partial^4 Y}{\partial \xi^4} + 4(\phi + \theta^2)\dfrac{\partial^2 Y}{\partial \xi^2} - 8\theta\beta\dfrac{\partial Y}{\partial \xi} + 4Y = 0, \\
\qquad\qquad \xi < -\dfrac{L}{2} \quad \text{or} \quad \xi > \dfrac{L}{2}, \\
\dfrac{\partial^4 Y}{\partial \xi^4} + 4[(\phi + (1+\alpha)\theta^2]\dfrac{\partial^2 Y}{\partial \xi^2} - 8\theta\beta\dfrac{\partial Y}{\partial \xi} + 4Y = 0, \\
\qquad\qquad -\dfrac{L}{2} \le \xi \le \dfrac{L}{2}.
\end{cases} \tag{a1}
$$

Here $Y = e^{m\xi}$ and $Y = e^{n\xi}$ are assumed and substituted into the two equations of eq. (a1), which leads to following equations:

$$
\begin{cases}
m^4 + 4(\phi + \theta^2)m^2 - 8\theta\beta m + 4 = 0, \\
\qquad\qquad \xi < -\dfrac{L}{2} \quad \text{or} \quad \xi > \dfrac{L}{2}, \\
n^4 + 4[(\phi + (1+\alpha)\theta^2]n^2 - 8\theta\beta n + 4 = 0, \\
\qquad\qquad -\dfrac{L}{2} \le \xi \le \dfrac{L}{2}.
\end{cases} \tag{a2}
$$

We assume that m_1, m_2, m_3, m_4 and n_1, n_2, n_3, n_4 are the complex roots for the above two quartic equations, respectively. Clearly, these roots satisfy the following identities:

$$
\begin{cases}
(m - m_1)(m - m_2)(m - m_3)(m - m_4) = 0, \\
\qquad\qquad \xi < -\dfrac{L}{2} \quad \text{or} \quad \xi > \dfrac{L}{2}, \\
(n - n_1)(n - n_2)(n - n_3)(n - n_4) = 0, \\
\qquad\qquad -\dfrac{L}{2} \le \xi \le \dfrac{L}{2}.
\end{cases} \tag{a3}
$$

The complex roots are also assumed to have the following forms of the real and imaginary parts [12]

$$
\begin{cases}
m_1 = a + ib_1, \\
m_2 = a - ib_1, \\
m_3 = -a + ib_2, \\
m_4 = -a - ib_2,
\end{cases} \tag{a4}
$$

and

$$
\begin{cases}
n_1 = c + id_1, \\
n_2 = c - id_1, \\
n_3 = -c + id_2, \\
n_4 = -c - id_2.
\end{cases} \tag{a5}
$$

Notice that the typos of $m_3 = a + ib_2$, $m_4 = a - ib_2$ terms were made in the Kenney's paper [12]. By substituting eqs. (a4) and (a5) into eq. (a3), the followings equations are derived:

$$
\begin{cases}
m^4 + (-2a^2 + b_1^2 + b_2^2)m^2 - 2a(b_2^2 - b_1^2)m \\
\quad + (a^2 + b_1^2)(a^2 + b_2^2) = 0, \quad \xi < -\dfrac{L}{2} \quad \text{or} \quad \xi > \dfrac{L}{2}, \\
n^4 + (-2c^2 + d_1^2 + d_2^2)n^2 - 2c(d_2^2 - d_1^2)n \\
\quad + (c^2 + d_1^2)(c^2 + d_2^2) = 0, \quad -\dfrac{L}{2} \le \xi \le \dfrac{L}{2}.
\end{cases} \tag{a6}
$$

By comparing the two equation sets of eqs. (a2) and (a6), the following equation sets are obtained

$$
\begin{cases}
-2a^2 + b_1^2 + b_2^2 = 4(\phi + \theta^2), \\
-2a(b_2^2 - b_1^2) = -8\theta\beta, \\
(a^2 + b_1^2)(a^2 + b_2^2) = 4,
\end{cases} \tag{a7}
$$

$$
\begin{cases}
-2c^2 + d_1^2 + d_2^2 = 4[(\phi + (1+\alpha)\theta^2], \\
-2c(d_2^2 - d_1^2) = -8\theta\beta, \\
(c^2 + d_1^2)(c^2 + d_2^2) = 4.
\end{cases} \tag{a8}
$$

From the first two equations of eqs. (a7) and (a8), the following equation sets are derived

$$
\begin{cases}
b_1^2 = 2(\phi + \theta^2) + a^2 - 2\dfrac{\theta\beta}{a}, \\
b_2^2 = 2(\phi + \theta^2) + a^2 + 2\dfrac{\theta\beta}{a},
\end{cases} \tag{a9}
$$

$$
\begin{cases}
d_1^2 = 2[(\phi + (1+\alpha)\theta^2] + c^2 - 2\dfrac{\theta\beta}{c}, \\
d_2^2 = 2[(\phi + (1+\alpha)\theta^2] + c^2 + 2\dfrac{\theta\beta}{c}.
\end{cases} \tag{a10}
$$

The following two equations are obtained by substituting eqs. (a9) and (a10) into the third equations of eqs. (a7) and (a8), respectively

$$
a^6 + 2(\phi + \theta^2)a^4 + \left[(\phi + \theta^2)^2 - 1\right]a^2 - \theta^2\beta^2 = 0, \tag{a11}
$$

$$c^6 + 2[(\phi + (1 + \alpha)\theta^2]c^4 + \left\{\left[\phi + (1 + \alpha)\theta^2\right]^2 - 1\right\}c^2$$
$$- \theta^2\beta^2 = 0. \tag{a12}$$

The above two sextic equations can be transformed into two cubic equations by simply letting $\delta = a^2$ and $\psi = c^2$

$$\delta^3 + 2(\phi + \theta^2)\delta^2 + \left[(\phi + \theta^2)^2 - 1\right]\delta - \theta^2\beta^2 = 0, \tag{a13}$$

$$\psi^3 + 2[(\phi + (1 + \alpha)\theta^2]\psi^2 + \left\{\left[\phi + (1 + \alpha)\theta^2\right]^2 - 1\right\}\psi$$
$$- \theta^2\beta^2 = 0. \tag{a14}$$

Mathematically, the cubic equations of eqs. (a13) and (a14) are the mechanism for the wavenumber bifurcations as presented in Figures 9, 10 and 13. It is noteworthy and interesting to mention that the large deflection of a structure also induces this cubic nonlinearity [49], which is responsible for the pitchfork bifurcation in the post-buckling analysis. Eq. (10), as a whole, is nonlinear though it consists of two linear governing equations for three domains. The very same cases are also encountered in the problems of the beam bending on a tensionless [35, 37] or a bilinear foundation [48].

The above two cubic equations of eqs. (a13) and (a14) can be further transformed into the following reduced forms [50]:

$$\Delta^3 + p_1\Delta + q_1 = 0, \tag{a15}$$

$$\Psi^3 + p_2\Psi + q_2 = 0. \tag{a16}$$

Here $\Delta = \delta + a_1/3$, $p_1 = -a_1^2/3 + b_1$, $q_1 = 2(a_1^3/3)^3 - a_1b_1/3 + c_1$ and $\Psi = \psi + a_1/3$, $p_2 = -a_2^2/3 + b_2$, $q_2 = 2(a_2^3/3)^3 - a_2b_2/3 + c_2$ with the following definitions

$$a_1 = 2(\phi + \theta^2), \; b_1 = (\phi + \theta^2)^2 - 1, \; c_1 = -\theta^2\beta^2;$$
$$a_2 = 2[(\phi + (1 + \alpha)\theta^2], \; b_2 = \left[\phi + (1 + \alpha)\theta^2\right]^2 - 1, \tag{a17}$$
$$c_2 = -\theta^2\beta^2.$$

The Q_is ($i = 1, 2$) are defined as follows:

$$Q_1 = \left(\frac{p_1}{3}\right)^3 + \left(\frac{q_1}{2}\right)^2, \; Q_2 = \left(\frac{p_2}{3}\right)^3 + \left(\frac{q_2}{2}\right)^2. \tag{a18}$$

The value of Q_i determines the three solution scenarios of the cubic equations [50]:

$Q_i > 0$: One real root, two complex conjugates.
$Q_i = 0$: Three real roots, at least two are equal.
$Q_i < 0$: Three real roots.

In all our computation, both Q_1 and Q_2 are always negative. As the results, the three roots of eqs. (a15) and (a16) are given as follows [50]:

$$\Delta_1 = 2\sqrt{-\frac{p_1}{3}}\cos\left(\frac{\alpha_1}{3}\right),$$
$$\Delta_2 = -2\sqrt{-\frac{p_1}{3}}\cos\left(\frac{\alpha_1 + \pi}{3}\right), \tag{a19}$$
$$\Delta_3 = -2\sqrt{-\frac{p_1}{3}}\cos\left(\frac{\alpha_1 - \pi}{3}\right),$$

$$\Psi_1 = 2\sqrt{-\frac{p_2}{3}}\cos\left(\frac{\alpha_2}{3}\right),$$
$$\Psi_2 = -2\sqrt{-\frac{p_2}{3}}\cos\left(\frac{\alpha_2 + \pi}{3}\right), \tag{a20}$$
$$\Psi_3 = -2\sqrt{-\frac{p_2}{3}}\cos\left(\frac{\alpha_2 - \pi}{3}\right).$$

Here α_1 and α_2 are defined as the following:

$$\alpha_1 = \cos^{-1}\left[\frac{-q_1}{2\sqrt{-(p_1/3)^3}}\right], \; \alpha_2 = \cos^{-1}\left[\frac{-q_2}{2\sqrt{-(p_2/3)^3}}\right]. \tag{a21}$$

Now the cubic equations of eqs. (a15) and (a16) are solved. Because a in eq. (a11) and c in eq. (a12) are required to be the real positive roots [12], which can only be satisfied by one of three cubic roots, a and c are given as follows:

$$a = \sqrt{\delta_3} = \sqrt{\Delta_3 - \frac{a_1}{3}}, \; c = \sqrt{\psi_3} = \sqrt{\Psi_3 - \frac{a_2}{3}}. \tag{a22}$$

With the above solutions of a and c, the wave numbers of b_1, b_2 and d_1, d_2 are now solved from eqs. (a9) and (a10). Then the solutions to the homogeneous equations of eq. (a1) are also obtained. A particular solution to the second equation of eq. (10) can be easily obtained as $Y_p = \gamma$. The solutions to eq. (10) are presented in eq. (11) by summing up both the homogeneous and particular solutions.